数理解析研究所講究録
第719巻 1990年 95-105

カルマン渦列の不安定と再配列

九大応力研　船越満明　(Mitsuaki Funakoshi)
九大応力研　烏谷　隆　(Takashi Karasudani)
九大応力研　星野スマ子　(Sumako Hoshino)

ABSTRACT

Breakdown and rearrangement of regular vortex streets in the wake of a circular cylinder are examined experimentally. The evolution of vorticity field is obtained using digital image processing for visualized flow fields. For $100 < R < 140$ (R is the Reynolds number based on the velocity U_0 and diameter of the cylinder) a primary vortex street evolves to a parallel shear flow of Gaussian profile due to anisotropic extension of the vortex regions. Subsequently a secondary vortex street of larger scale appears. The wavelength of it is within the instability region in the linear stability theory for the above velocity profile. The wavelength is, however, fairly smaller than that of the most unstable mode. Finally it is shown that the vortex regions in the primary and secondary vortex street move at the speeds $0.15U_0 \sim 0.19U_0$ and $0.05U_0 \sim 0.10U_0$, respectively, relative to the fluid at infinity.

It is well known experimentally that regular vortex streets (Kármán vortex streets) are generated for $40 \lesssim R \lesssim 200$ when a circular cylinder of diameter d moves in a fluid at velocity U_0. Here $R = U_0 d/\nu$, and ν is the kinematic viscosity of the fluid. Taneda[1] showed that this primary vortex street breaks down at some downstream distance x_0 from the cylinder and that a secondary vortex street subsequently appears for $50 \lesssim R \lesssim 200$. (Honji[2] obtained the dependence of x_0/d on R.) It is, however, not resolved clearly what mechanism is dominant in the above breakdown and rearrangement of vortex streets. Taneda[1] and Cimbala *et al.*[3] claimed that the above process can be explained by the theory of hydrodynamic stability for a parallel shear flow. Matsui and Okude[4] claimed that pairing of vortex regions is a dominant mechanism.

The main purpose of this letter is to make clear the evolution of vortex regions associated with the above breakdown and rearrangement. In order to experimentally examine this problem, we used digital image processing for visualized flow fields.

Figure 1 is a schematic diagram of our apparatus. Experiments were carried out using two water tanks with glass sides. The sizes of them are 400 cm long, 40 cm deep, and 40 cm wide ; 700 cm long, 40 cm deep, and 60 cm wide. Carriages to which a model is fixed upright move uniformly along rails mounted horizontally over the water tanks. A stainless steel circular cylinder of diameter 1.0 cm was used as a model, and a scrap of flexible tape was attached at the bottom end of the cylinder in order to diminish end effects.

The working fluid is water containing polyethylene particles.

The particles of diameter 75 ~ 150 μm, coated with a bond (Alone-alpha) in order to make their density same as water's one, were suspended for flow visualization. They were illuminated horizontally at the height 25 cm from the bottom by sheets of light from slide projectors. The thickness of the sheets was about 5 mm at the position of a model. Movements of the particles were recorded by a video camera. Elapsed time also was recorded on a video image.

Two types of experiments have been performed for $100 < R < 140$. The first one was made using the shorter tank with the video camera fixed at 1.5 m ahead the initial position of a model. The second one was made using the longer tank with the video camera moved at velocity U_1, which is comparable to that of primary vortex streets. Each experiment was repeated over 10 times, and image data having good contrast and adequate particle density were analyzed.

Velocity and vorticity fields were computed from each image data by means of the following procedure. When we want to obtain the fields at time T, two instantaneous images of polyethylene particles at $T_1 = T - \Delta T$ and $T_2 = T + \Delta T$ and a track image for the time from T_1 to T_2 are generated on an image processor (NEXUS 6400) through an A/D converter. These three digital images are reduced to binary images with a threshold value b. Then velocity data are computed from the positions of the ends of available pathlines during appropriately small time $2\Delta T$ in the track image. Here the data acquisition is made automatically with removing intersecting pathlines. Furthermore, pathlines of particles which appear later than T_1 or disappear earlier than T_2, whose

ratio is fairly small, are also removed automatically. We used a few values of b for each image in order to obtain as many velocity data as possible. We usually obtained 300 ~ 600 data for each image.

Velocities at lattice points of a square lattice of spacing l, which is $0.5d$ ~ $0.6d$, are computed from the above velocity data by an interpolation method. Figure 2 shows one example of original velocity data (thin lines) and velocities at lattice points (thick lines). It is found that the interpolation method works well.

Here we use x and y as the coordinates in the longitudinal and transverse directions, respectively. The origin of the coordinate system is located at the backward edge of the cylinder. The vorticity ω at each lattice point is computed from the data of velocities (u, v) in the (x, y) directions at four neighbouring lattice points using a centered difference.

Next the evolutions of vorticity and velocity fields obtained by the above method are discussed. In order to specify each image, we introduce a variable L defined by the x value of the center of the image. Figure 3 shows the evolution of vorticity field. Contour lines for positive and negative vorticities are expressed by solid and dashed lines, respectively. It should be noted that the contour lines are drawn based on the values normalized with the largest absolute value of vorticity of each image, which decreases with the increase of L. Both Fig.3(a) for R = 140 (and U_1 = 0) and Fig.3(b) for R = 106 (and $U_1 = 0.2U_0$) show that primary vortex streets evolve to parallel shear flows due to anisotropic extension of vortex regions. Furthermore, subsequent appearance of secondary vortex streets of larger scale is found.

In order to show this process more clearly, we computed transversally integrated vorticity Ω for several L. Figure 4 shows three examples of the x-dependence of Ω normalized with Ω_N, which is computed by the longitudinal averaging, over all x in an image, of transversally integrated absolute value of vorticity. Transitions among the states of primary vortex street, parallel shear flow, and secondary vortex street of larger longitudinal scale, are easily found.

In the extension process of vortex regions in primary vortex streets, the effect of viscous diffusion does not seem dominant. One reason for it is that the time required for the diffusion of vorticity over the representative longitudinal length scale of primary vortex streets is estimated as about 25 times as long as the time spent for the extension in the experiments. Another reason is the anisotropic extension of vorticity. Therefore, it is suggested that an inviscid theory may explain most of this extension process. Using a discrete vortex method, Tsuboi and Oshima[5] showed that the evolution of a vortex street to a parallel shear flow can be found in an inviscid theory. This result is consistent with our suggestion.

Next it seems interesting to compare the wavelength λ_s of the secondary vortex street with the result of the theory of hydrodynamic stability for parallel shear flows, since the observed velocity field becomes approximately parallel just before the appearance of the secondary vortex street. The longitudinal velocity profiles obtained by averaging over all x in each image and by subtracting the velocity at infinity, are shown in Fig.5 (thick lines) for L yielding approximately parallel shear flow. Best-fitted

Gaussian profiles $u_0\exp(-\alpha^2 y^2)$ are also shown there (thin lines). The observed velocity profiles are well approximated by the Gaussian ones. The local Reynolds numbers R_l based on u_0 and α^{-1} of these Gaussian profiles are 71 and 54 for R = 140 and R = 106, respectively. These values are much larger than the critical value of R_l, 4.5, in the linear stability theory. The observed wavelength λ_s is $7.5d \sim 8.5d$ for R = 140. According to the computation by Fujimura *et al.*,[6] the mode of this wavelength is unstable in the linear theory. The mode of the largest growth rate, however, has wavelength $12.5d$, which is fairly larger than λ_s. Therefore, the generation of the secondary vortex street can not be explained only by the direct application of the linear stability theory to the observed parallel shear flow. This problem may be resolved by the consideration of the downstream development of a mean velocity profile.

Finally, the movement of the regions of large vorticity is examined. The speed of vortex regions in the primary vortex street in the longitudinal direction relative to the fluid at infinity is $0.18U_0 \sim 0.19U_0$ for R = 140 and is $0.15U_0 \sim 0.18U_0$ for R = 106. Vortex regions in the secondary vortex street move at the lower speed of $0.05U_0 \sim 0.10U_0$ for these values of R. Movements of the vortex regions are expressed by arrows in Fig.3.

In conclusion it can be said that for $100 < R < 140$ the primary vortex street evolves to a parallel shear flow of Gaussian profile due to anisotropic extension of the vortex regions. Subsequently the secondary vortex street of larger scale appears. The wavelength of it is within the instability region in the linear stability theory for the above velocity profile. The wavelength is, however, fairly

smaller than that of the most unstable mode. Moreover, the vortex regions in the primary and secondary vortex street move at the speeds $0.15U_0 \sim 0.19U_0$ and $0.05U_0 \sim 0.10U_0$, respectively, relative to the fluid at infinity.

References

1) S.Taneda : J. Phys. Soc. Jpn. **14** (1959) 843.

2) H.Honji : J. Phys. Soc. Jpn. **55** (1986) 2897.

3) J.M.Cimbala, H.M.Nagib, and A.Roshko : J. Fluid Mech. **190** (1988) 265.

4) T.Matsui and M.Okude : *Structure of Complex Turbulent Shear Flow IUTAM Symposium, Marseille, 1982* (Springer, Berlin, 1983) p.156.

5) K.Tsuboi and Y.Oshima : *Proc. Computational Fluid Dynamics, Tokyo, 1985*, ed. K.Oshima, p.230.

6) K.Fujimura, S.Yanase, and J.Mizushima : Fluid Dyn. Res. **4** (1988) 15.

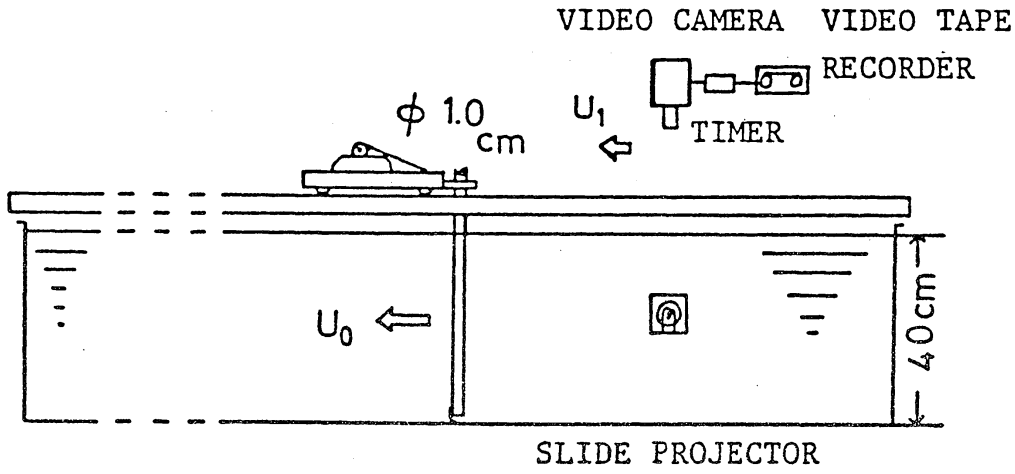

Fig.1 Schematic diagram of the apparatus. U_0 is the velocity of a cylinder, U_1 the velocity of a video camera.

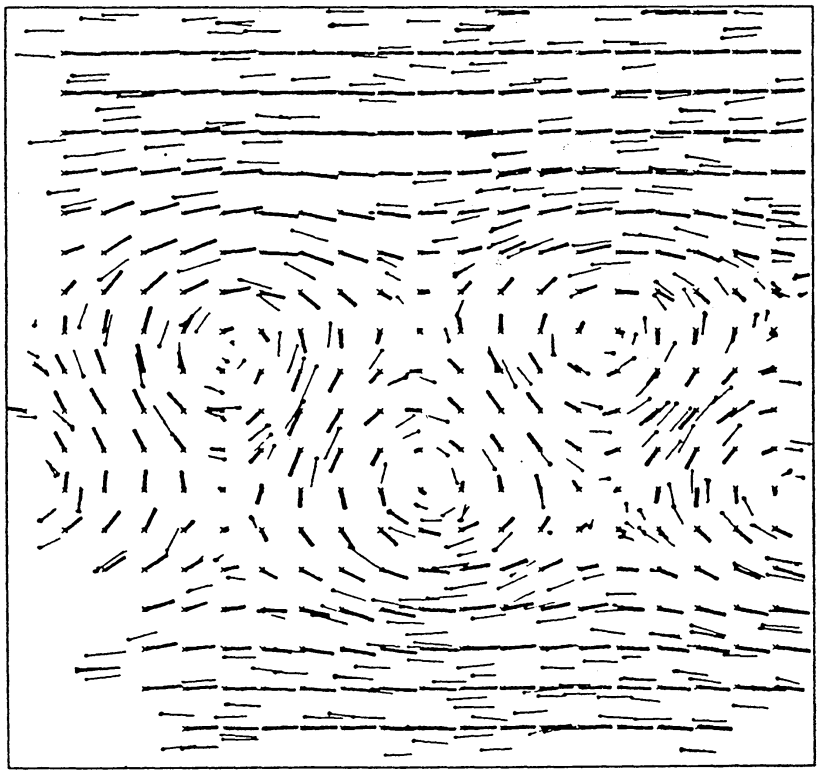

Fig.2 Original velocity data (thin lines) and velocities at lattice points (thick lines).

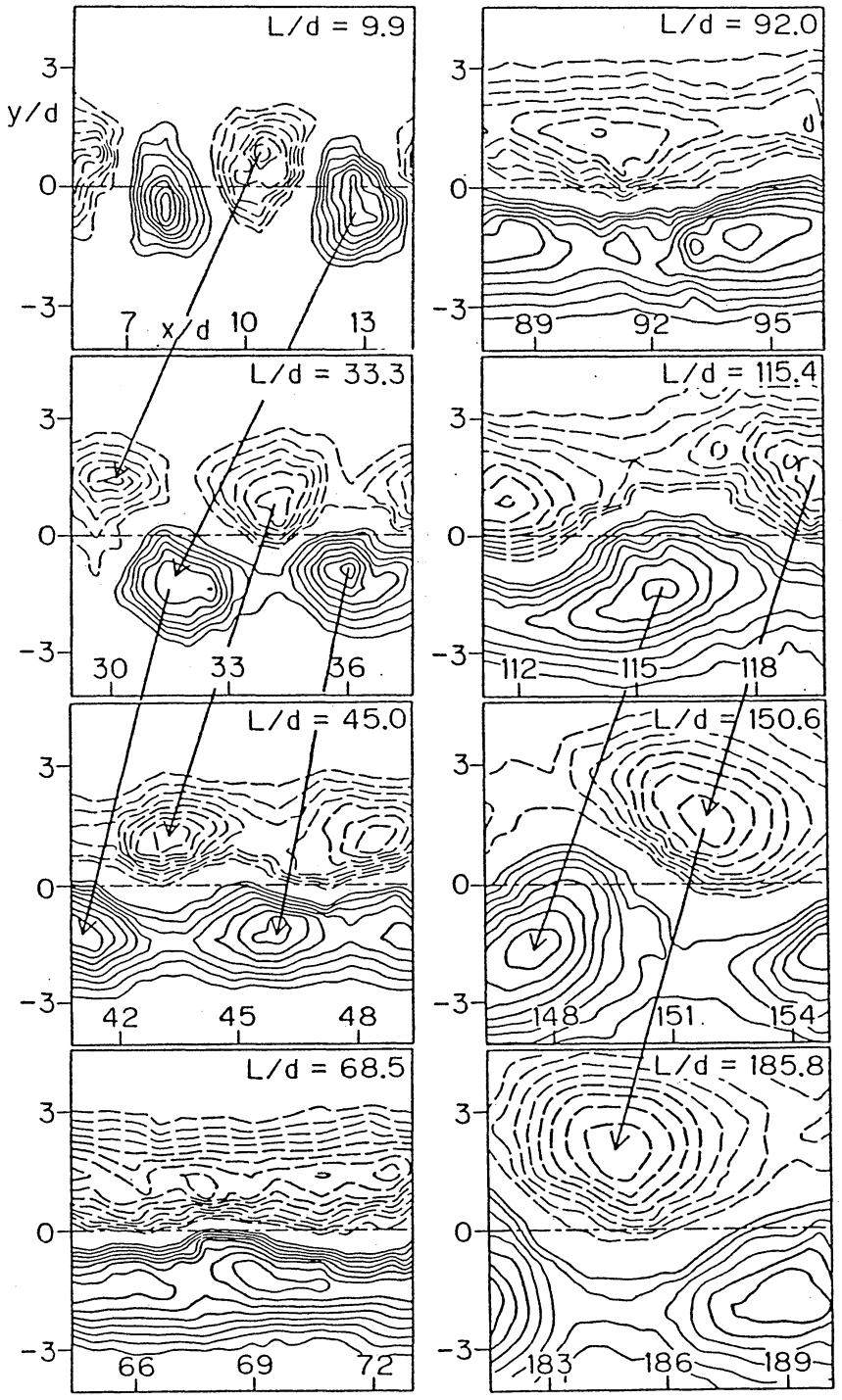
L/d = 9.9
L/d = 92.0
L/d = 33.3
L/d = 115.4
L/d = 45.0
L/d = 150.6
L/d = 68.5
L/d = 185.8
y/d
x/d
3
0
-3
7
10
13
89
92
95
30
33
36
112
115
118
42
45
48
148
151
154
66
69
72
183
186
189

Fig.3(a)

(b)

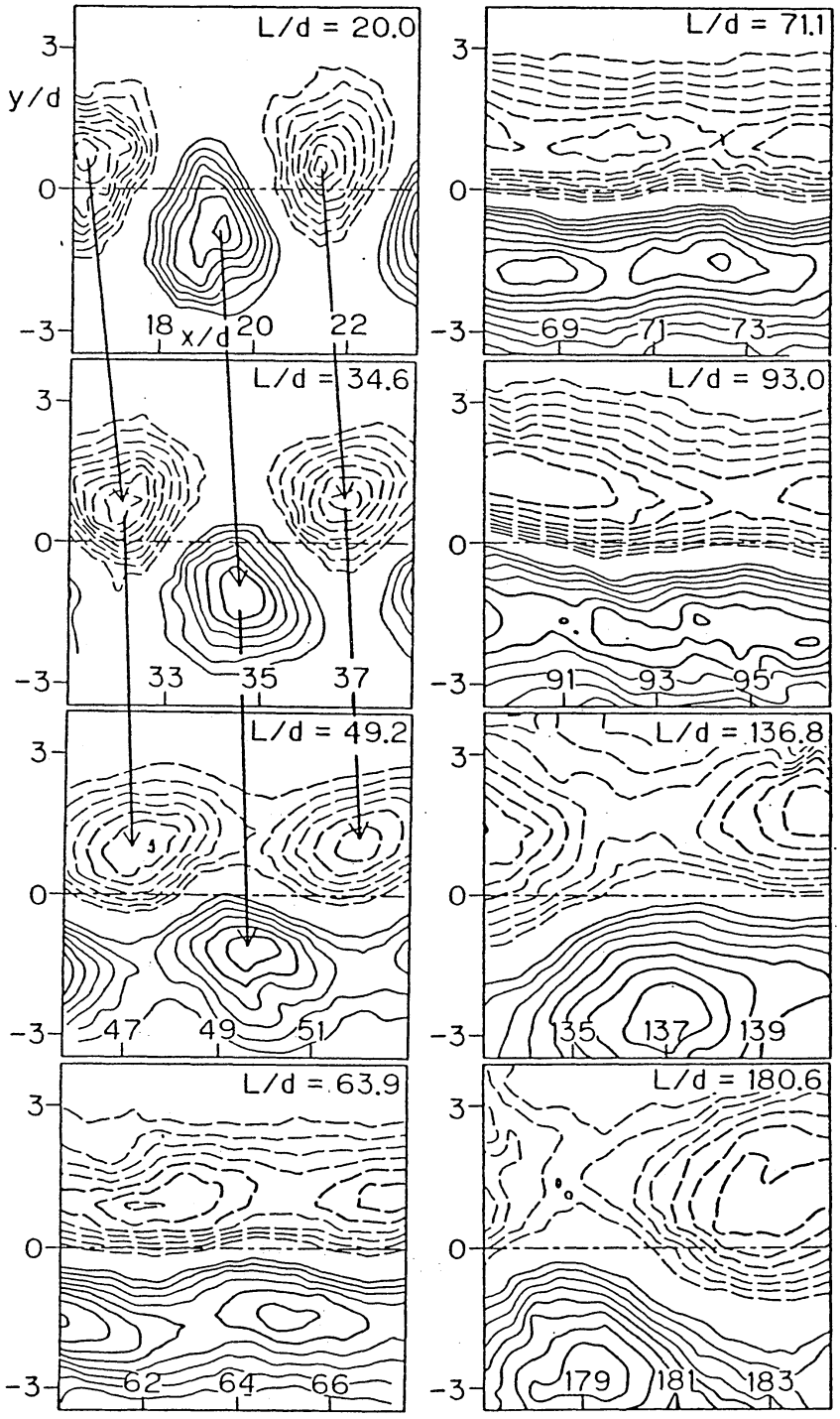

Fig.3 Evolution of vorticity field. Contour lines for positive vorticity (solid lines) and for negative vorticity (dashed lines) are drawn based on the values $\pm 0.2\omega_{max}$, $\pm 0.3\omega_{max}$, ···, $\pm 0.9\omega_{max}$. Here ω_{max} is the maximum absolute value of the vorticity for each L. Movements of the vortex regions are denoted by arrows. (a) : R = 140, U_1 = 0. (b) : R = 106, $U_1 = 0.2U_0$.

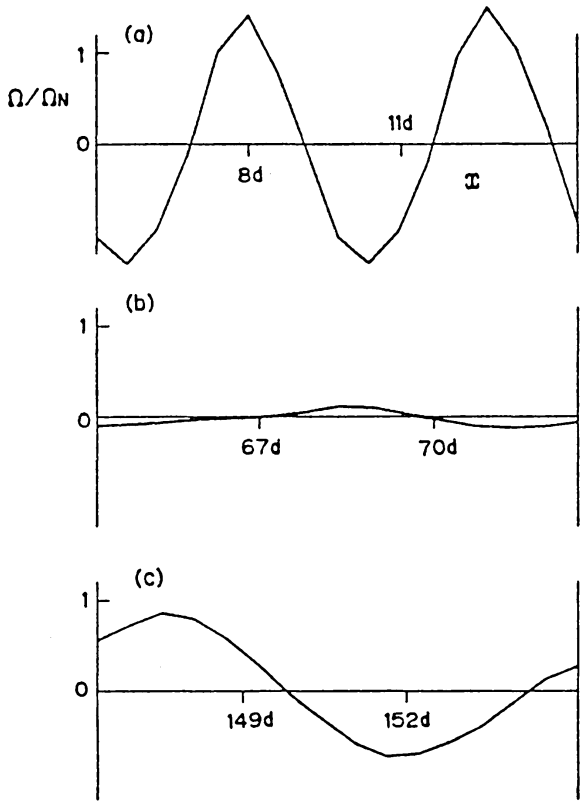

Fig.4 Evolution of normalized transversally integrated vorticity Ω/Ω_N. R = 140. (a) L/d = 9.9, (b) L/d = 68.5, (c) L/d = 150.6.

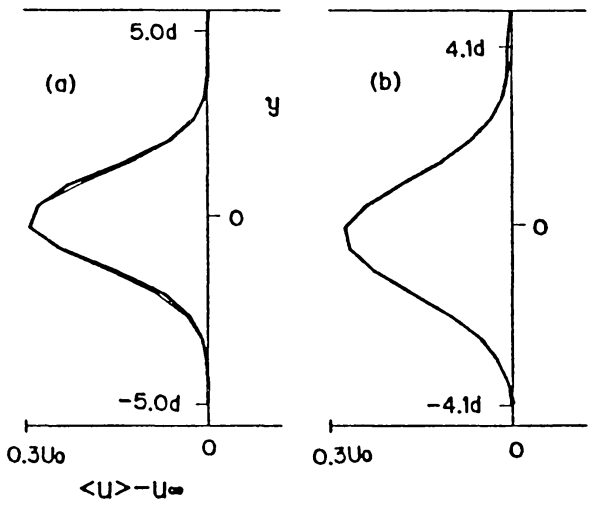

Fig.5 Longitudinal mean velocity profiles in the experiments (thick lines) and best-fitted Gaussian profiles (thin lines). (a) R = 140, L/d = 68.5, (b) R = 106, L/d = 71.1.